Available online at www.sciencedirect.com
ScienceDirect
Planetary and Space Science 58 (2010) 166–181
Planetary and Space Science
www.elsevier.com/locate/pss

SERENA: A suite of four instruments (ELENA, STROFIO, PICAM and MIPA) on board BepiColombo-MPO for particle detection in the Hermean environment

S. Orsini[a,*], S. Livi[b], K. Torkar[c], S. Barabash[d], A. Milillo[a], P. Wurz[e], A.M. Di Lellis[f], E. Kallio[g], the SERENA team[1]

[a]*INAF-Istituto di Fisica dello Spazio Interplanetario, Rome, Italy*
[b]*Southwest Research Institute, San Antonio, TX, USA*
[c]*Space Research Institute, Austrian Academy of Sciences, Graz, Austria*
[d]*IRF, Swedish Institute of Space Physics, Kiruna, Sweden*
[e]*Physicalisches Insitut, Space Research & Planetary Sciences, University, Bern, Switzerland*
[f]*AMDL s.r.l., Rome, Italy*
[g]*Finnish Meteorological Institute, Helsinki, Finland*

Received 19 February 2008; received in revised form 26 August 2008; accepted 4 September 2008
Available online 11 October 2008

Abstract

'Search for Exospheric Refilling and Emitted Natural Abundances' (SERENA) is an instrument package that will fly on board the BepiColombo/Mercury Planetary Orbiter (MPO). It will investigate Mercury's complex particle environment that is composed of thermal and directional neutral atoms (exosphere) caused by surface release and charge-exchange processes, and of ionized particles caused by photo-ionization of neutrals as well by charge exchange and surface release processes. In order to investigate the structure and dynamics of the environment, an in-situ analysis of the key neutral and charged components is necessary, and for this purpose the SERENA instrument shall include four units: two neutral particle analyzers (Emitted Low Energy Neutral Atoms (ELENA) sensor and Start from a Rotating FIeld mass spectrometer (STROFIO)) and two ion spectrometers (Miniature Ion Precipitation Analyzer (MIPA) and Planetary Ion Camera (PICAM)). The scientific merits of SERENA are presented, and the basic characteristics of the four units are described, with a focus on novel technological aspects.

Keywords: Mercury's exosphere; Magnetospheric plasma; Sun–Mercury interaction; Particle detectors

1. Science merits

1.1. The Hermean environment

The environment surrounding the planet Mercury is a complex system, generated by the coupling between the solar wind (SW), magnetosphere, exosphere and surface, so that a comprehensive description of its characteristics and dynamics cannot avoid a detailed analysis of all these four 'elements' (e.g. Milillo et al., 2005; Orsini et al., 2007).

Fig. 1 briefly describes the basic features of the Hermean environment. The planet has an intrinsic magnetic field, significantly weaker than the terrestrial one, so that the SW plasma and its frozen-in interplanetary magnetic field (IMF) can interact with it, generating a shock interface very close to the planet surface.

SW plasma can enter into the magnetosphere. The main access mechanism is similar to substorm trigger at the Earth, that is the magnetic reconnection of the IMF with the planetary magnetic field permits the plasma entry through the cusps (Kabin et al., 2000; Kallio and Janhunen, 2003; Massetti et al., 2007; Sarantos et al., 2007). In the case of Mercury, the weak internal magnetic field implies large-ion giroradii compared to the planet's

*Corresponding author.
E-mail address: stefano.orsini@ifsi-roma.inaf.it (S. Orsini).
[1]See Appendix A.

0032-0633/$ - see front matter © 2008 Elsevier Ltd. All rights reserved.
doi:10.1016/j.pss.2008.09.012

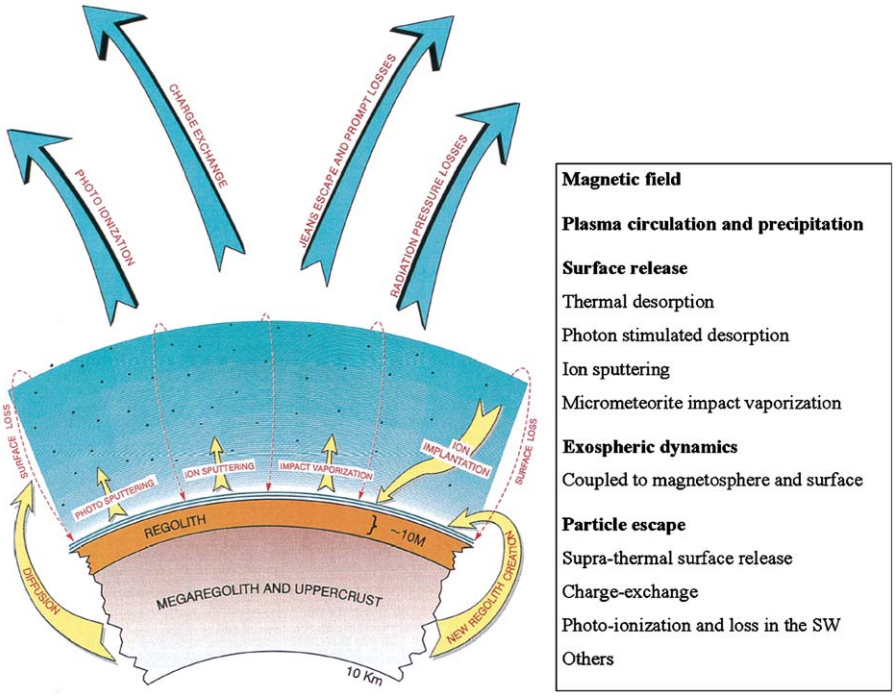

Fig. 1. Features of the Hermean Environment (from Killen et al., 2004b).

size. Hence, especially in high SW pressure conditions, the particles can enter directly through the magnetopause (Kallio and Janhunen, 2003; Massetti et al., 2007).

Inside this small-scale magnetosphere, charged particles may circulate, but as the ions have large gyroradii compared to the planet's size, in most regions of the magnetosphere the adiabatic approximation is not valid. In large areas, the SW impacts on the surface itself, generating neutral particle emission via ion sputtering (sputtering also creates ions on a percent level, not just neutrals). This release process combines with other processes such as solar radiation and micrometeoroid impacts. The bulk of these surface released particles generate a tenuous collisionless gas cloud, called an exosphere. The dynamical behavior of this exospheric gas, strongly coupled with the planet surface and the Hermean magnetosphere, causes neutral particle precipitation onto the surface as well as escape towards space. The photo-ionization lifetime in the Mercury dayside is short enough to validate the idea that an ionized population of planetary origin may reside in the planet's environment.

1.2. Science objectives

'Search for Exospheric Refilling and Emitted Natural Abundances' (SERENA) is an instrument package that will fly onboard Mercury Planetary Orbiter (MPO), and that will be able to provide information about the whole surface–exosphere–magnetosphere system, as well as about the processes involved in this system, subjected to strong interaction with the SW and the interplanetary medium. In the Hermean environment the interaction between energetic particles, solar radiation and micrometeorites with the Hermean surface gives rise to both thermal and energetic neutral populations in the near-planet space. Such populations will be recorded by the SERENA neutral particle analyzers, namely Emitted Low Energy Neutral Atoms (ELENA) sensor and Start from a Rotating FIeld mass spectrometer (STROFIO) (form a Greek word meaning 'rotate' it is a neutral gas mass spectrometer based on a rotating electric field). The photoionized or charged component of the surface release processes as well as the precipitating and circulating ions in the Hermean magnetosphere will be recorded by the SERENA Ion Spectrometers, namely Planetary Ion Camera (PICAM) and Miniature Ion Precipitation Analyzer (MIPA). In particular, ELENA will observe the sputtered high energy atoms (SHEA) escaping from the surface of Mercury, investigating the related involved processes; STROFIO will provide the thermal exospheric gas composition; PICAM will permit to derive the exo-ionosphere extension and composition, and the close-to-planet magnetospheric dynamics; MIPA will detect the plasma precipitation toward the surface and ions energized and transported throughout the environment of Mercury.

SERENA will address a number of objectives, as listed in the following.

1.2.1. Chemical and elemental composition of the exosphere

It is expected that the six observed elements (H, He, O, Na, K and Ca) (e.g. Milillo et al., 2005; Killen and Ip, 1999) may constitute only a small fraction of Mercury's exosphere, because at the surface the total pressure, derived from the sum of these known species, is almost two orders

of magnitude less than the exospheric pressure of approximately 10^{-10} mbar, obtained by the Mariner 10 occultation experiment (Fjelbo et al., 1976). Radar-bright regions have been discovered at the poles, attributed to volatile deposits (water or sulphur) in permanently shadowed craters. The quantification of different exospheric components is crucial for the determination of the environment composition since the neutral component is the primary constituent of the Hermean environment. Up to now, attempts to perform such quantification only come from the few Mariner 10 measurements, and from some ground-based observations. Determination of aggregation status of atoms and molecules in the exosphere is important for the better understanding of the occurring processes. The STROFIO sensor is unique in its capability to perform quantitative analysis and resolve exospheric gas chemical and elemental composition in the dayside as well as in the night side. Moreover, these in-situ measurements will allow a better evaluation of the local gas characteristics and dynamical behavior, to be complemented by the more global remote sensing data gained via UV signal detection by another instrument onboard MPO, named PHEBUS (Chassefiere et al., 2009).

1.2.2. *Exo-ionosphere composition and distribution*

The ions of planetary origin (like He^+, $Na^+ + Mg^+$, $O^+ + OH^+$, Si^+, S^+, $K^+ + Ca^+$) have recently been observed by MESSENGER in the night side magnetosphere (Zurbuchen et al., 2008). They are probably present, especially in the dayside hemisphere due to photoionisation and ion-sputtering processes (e.g. Milillo et al., 2005). The MPO orbit, being close to the planet, and the good duty cycle provided by 3-axis stabilization will permit PICAM to obtain continuous measurements of these ions, enabling a detailed composition measurement. Along the MPO orbit at low altitude, PICAM will be able to detect ionized particles created in the nearby regions; hence, they maintain, at least partially, the information about their generation process. The quantification of the ion component will provide useful information for the unsolved problems of the presence of an exo-ionosphere at Mercury. With a high sensitivity, the wide FOV and the mass resolution PICAM will provide us with a complete composition analysis of the Hermean plasma envelope.

Coupling between exo-ionosphere and exosphere, and its dependence on external conditions can be examined by estimating the neutral (STROFIO) to ion (PICAM) density ratios. Such measurements will also be useful, provided that all the ionization processes are well constrained, for taking highly needed experimental data for the photo-ionization rates at Mercury, which are still debated within the community (especially for some atoms and small molecules).

1.2.3. *Surface emission rate and release processes*

A central problem for understanding the evolution of solar system bodies is the role played by the solar radiation (both electromagnetic and corpuscular) and micro-meteorite bombardment in controlling mass losses through surface release (Killen and Ip, 1999). The rate of surface ageing by thermal desorption (TD), photon-stimulated desorption (PSD), and

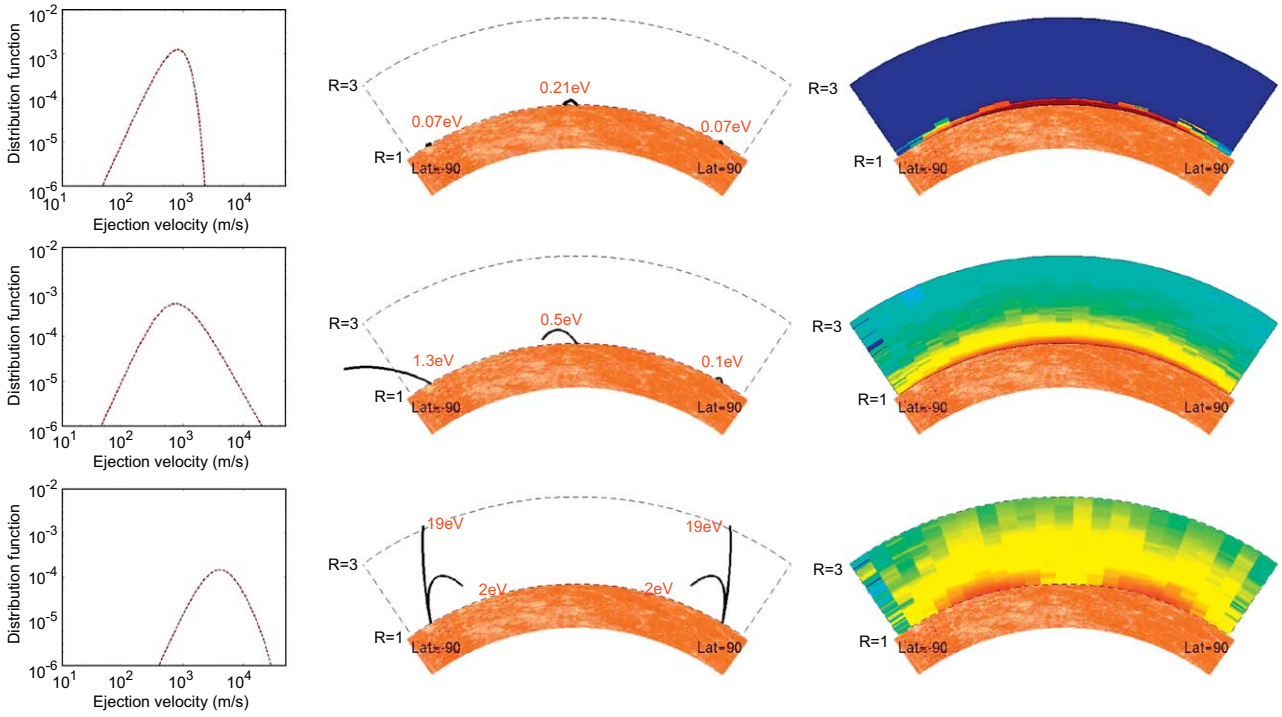

Fig. 2. Schematics of a Monte Carlo model simulation at Mercury, for different release processes. From the left column: energy spectra of the source process, sample trajectories, and simulated exosphere profiles (based on Mura et al., 2007a). Top row: TD; middle row: PSD; bottom row: ion sputtering. The planetary surface (in brown) represents a cut from −90° to 90° of latitude; the curvature is not to scale.

space weathering by ion-sputtering and micrometeoroid impact vaporisation is particularly relevant at Mercury. As schematically shown in Fig. 2, different release processes produce particles within different energy ranges (Wurz and Lammer, 2003). Protons precipitating onto the surface can also induce back-scattering process. In this case, the proton, after several scattering inside the first monolayers of the surface, experiences a back-scattering collision. Once back-scattered, the proton has to pass back through the surface again and eventually is emitted from the surface. During the multiple scattering a portion of energy and flux is lost. For an incoming monochromatic proton flux of energy E_i, the back-scattering energy spectra shows, in general, a continuous profile between 0 and E_i. These back-scattered atoms have similar directions with those of the sputtered ones, nevertheless they can be easily discriminated from them since they are mostly light particles (Hydrogen) and, hence, they have higher velocities. Observations of the gas evolving from the planet are of crucial importance to identify and to localize the different physical processes acting onto the surface as well as to estimate their relative efficiencies. Different release processes can have different efficiencies as a function of latitude and longitude at Mercury due to varying surface compositions and external conditions, such as solar irradiance or plasma precipitation. Moreover, observations of time scale of density variation could provide us with the signature of the active release process. In fact, while the TD and PSD are quasi-stationary processes (varying along the Mercury's orbit and according to the surface composition), the ion-sputtering process exhibits time scales typical of magnetospheric dynamics (tens of minutes). Hence, the detection of exospheric neutral particles over the whole energy range of each process, to be performed by STROFIO and ELENA, will allow us to identify the process responsible for their generation. In order to determine the emitting area on the surface, given the ballistic trajectories of the surface-released particles, we can assume that the ram pointing STROFIO detection will refer to a circular area whose radius is of the same order of magnitude of distance from the planet; while the surface mapping of the more energetic particles, SHEA, detected with high angular resolution by the nadir-pointing ELENA, permits to image the ion-sputtered emission with a resolution of 10 s km. Moreover, the correlation of the ELENA sputtered neutral flux with the MIPA plasma precipitation simultaneous measurements will provide information about the effectiveness of this process. In order to perform a full investigation of the ion-sputtering process, information about precipitating ion flux, surface composition and mineralogy should be known together with the released particles analysis (energy and composition). While the composition and mineralogy can be provided by other BepiColombo instruments, the precipitating fluxes are highly variable and need a simultaneous monitoring. The magnetic field measurements by the magnetometer on board MPO will help in the reconstruction of the ion trajectory foot prints. This reconstruction is subjected to an indetermination caused by drift and electromagnetic variations. Anyway, the scale length of the surface area interested by the precipitating flux is large enough to allow correlation between ion and neutral observations within this indetermination. Finally, with ELENA, STROFIO and MIPA it will be possible to map the location of the release processes on the surface, obtain an imaging of the surface loss rate and evaluate the efficiency of each process as a function of external conditions.

1.2.4. *Plasma precipitation rate*

As shown in the examples of Fig. 3, the SW ions entering in the magnetosphere: (a) partially reach the planet's surface and cause ion sputtering, hence producing neutral

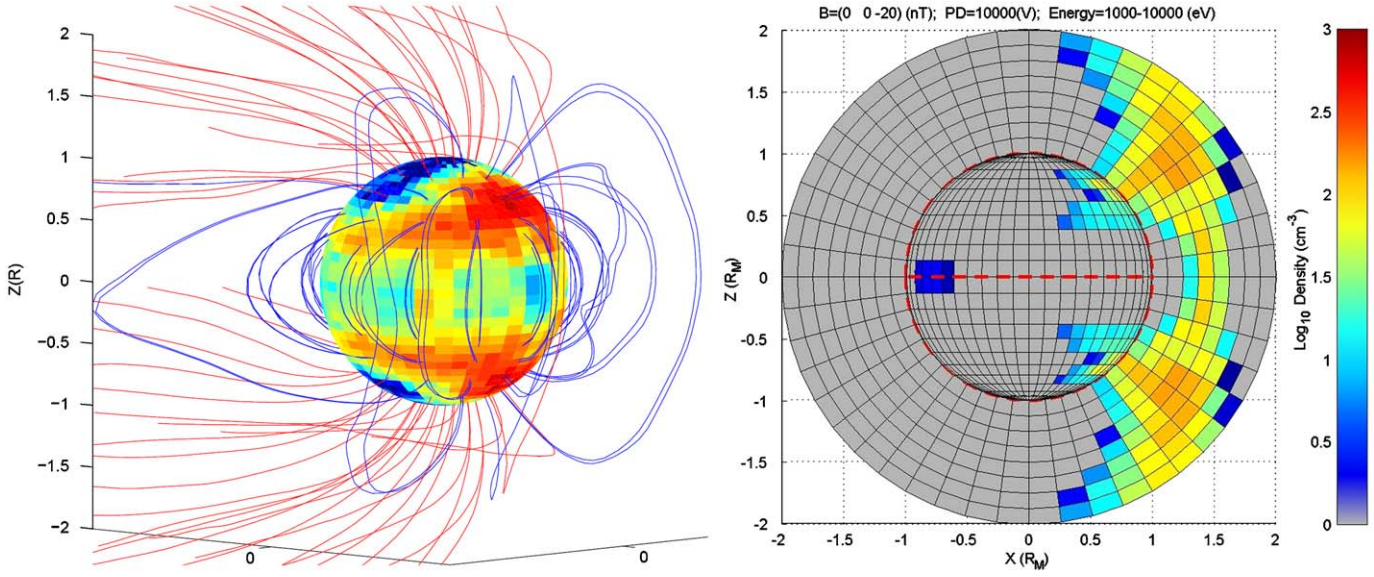

Fig. 3. Examples of proton precipitation patterns on the dayside of Mercury, as modeled by Kallio and Janhunen (2003) (*left panel*), and Mura et al. (2005) (*right panel*).

atoms and ions with energies up to hundreds of eV; (b) partially are diffused toward closed field lines and circulate in the magnetosphere; (c) partially exchange their charge with the thermal exospheric atoms, producing a Hydrogen-ENA (H-ENA) signal in the keV range. The intense flux of SW origin toward the planet (Massetti et al., 2003; Kallio and Janhunen, 2004; Mura et al., 2005) will be monitored by MIPA.

The precipitating planetary heavy-ion fluxes are lower with respect to precipitating SW fluxes, but they play a more important role in the night side where the SW contribution is probably negligible. Simulations show that planetary Na^+ ions may convect to the night side, where they are subjected to acceleration processes, and eventually they may hit the surface, causing a second generation of ion-sputtering process (Delcourt et al., 2003; Delcourt and Seki, 2006). The quantitative estimate of this signal is difficult because ions move along field lines, but in any case both MIPA and PICAM observations are needed to monitor this process.

In summary, MIPA will measure the flux of loss-cone-precipitating particles at Mercury that could be back-traced to the originating SW source. These particles could also be forth-traced to the surface to identify the ion-sputtering locations, source of neutral and ion emission. The identification of the composition and energy distribution of the planetary ion flux impacting the surface can be achieved by joint analysis of MIPA and PICAM.

1.2.5. Particle loss rate from Mercury's environment

The SHEA products of the release processes as well as the charge-exchange ENA, are mainly created close to the surface and carried outward of the planetary environment due to their high velocity that exceeds the escape velocity. Directional neutral measurements are crucial for evaluating the mass loss from the Hermean environment. The ions produced at thermal energies are energized and become part of the magnetospheric ion populations, together with the SW plasma entering through the cusp regions; the magnetospheric plasma partially impacts on the surface; hence, these particles are absorbed by the surface at specific latitudes and are redistributed over the planetary surface; on the other hand, part of the magnetospheric plasma is eventually lost to the SW (see Ip, 1997; Delcourt et al., 2003; Leblanc et al., 2003; Killen et al., 2004a; Delcourt and Seki, 2006 for detailed descriptions of the features listed above). Ion measurements are important for the planetary global mass loss estimation and provide key information on the formation and erosion of Mercury's neutral exosphere. Such processes produce a global particle loss rate from the planet that can be derived from the measurements performed by ELENA and PICAM, thus providing crucial information for deriving the past and present evolution of the planet.

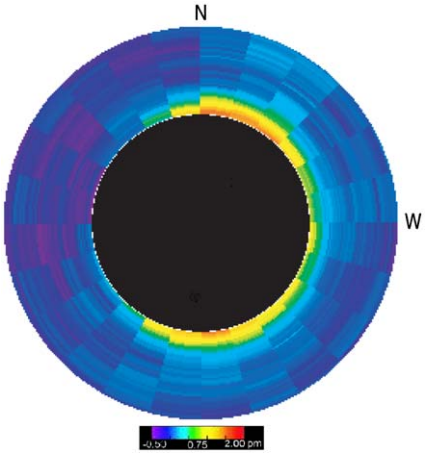

Fig. 4. Distribution of sodium D_2 absorption around the disk of Mercury seen in transit across the Sun. Concentrations of sodium vapor exist at high north and south latitudes. Sodium absorption is seen along the west equatorial limb (dawn), but not along the east equatorial limb (dusk). The true anomaly angle was 149.2° and radiation acceleration was 49.3 cm/s^2, or about 13.2% of surface gravity (from Schleicher et al., 2004).

1.2.6. Gas density profile asymmetries

The measurements of the spatial distributions of the neutrals are a possible way to understand the ejection processes that lead to these distributions and to have information about the history of the particles during their trajectories (e.g.: dissociation, acceleration, etc.). Moreover, asymmetries, induced by strong thermal variations, between different latitudes, day/night, dawn/dusk sides and perihelion/aphelion are expected in the Hermean exospheric density (Potter et al., 2006). The available ground-based observations confirm the existence of strong asymmetries (see Fig. 4), but cannot provide the necessary details for correctly interpreting this feature. STROFIO will be able to observe these asymmetries. It will be of particular interest to analyze the altitude profiles for different species released via different release processes, for example it will be useful to compare the density profile of Na and Ca (Killen et al., 2005) or Mg.

1.2.7. Further scientific goals

Due to the strong link between the exosphere and the surface, by measuring neutrals and ions at relatively low altitudes, SERENA will offer the possibility to get information about the composition of the upper surface. Such information should be compared to the other analyses of the surface composition, e.g. made with MPO/MIXS.

At higher MPO altitudes, PICAM will sense the ions that drift inside the magnetosphere, once accelerated under the action of electric and magnetic fields. Near the MPO apocentre, on the dayside or on the flanks, PICAM and MIPA will monitor a significant portion of the magnetosphere, and the way it acts on the SW ions and on planetary pick-up ions captured by the SW and convected with the SW to the planet. This information, in combination with the magnetic field data by MAG and plasma and field measurements onboard MMO, will help in understanding the structure and dynamics of the magnetosphere of Mercury.

The MPO spacecraft will be in both the unperturbed SW and the fore-shock for some time periods within the mission lifetime. In these conditions, MIPA and PICAM will perform SW plasma measurements and MAG magnetic field data will be useful in this context to define the particle trajectories.

In the following, an example of possible measurements by the SERENA package is depicted in the case of a coronal mass ejection (CME) arrival at Mercury. In this case, if MPO is located in the dayside magnetosphere, at mid-latitudes, a specific sequence of events will be monitored by the SERENA units:

- intensification of the SW flux (one or two orders of magnitude);
- MIPA detection of precipitating particles;
- the SW ions enter inside the cusps, partly diffuse and circulate inside the Hermean magnetosphere, and partly precipitate toward the surface producing ion-sputtering (e.g. Massetti et al., 2007; Kallio and Janhunen, 2003) and PSD yield enhancements (Mura et al., 2008; Sarantos et al., 2008);
- neutral particles are emitted by ion sputtering (e.g. Massetti et al., 2003; Mura et al., 2005);
- the SHEA are observed at high angular resolution by the nadir-pointing ELENA sensor;
- refractories and volatiles neutral atoms released by ion sputtering at lower energies and volatiles neutral atoms released by enhanced PSD are detected by the STROFIO sensor;
- enhanced fluxes of phtoionized particles and ions directly released from the surface by ion sputtering are detected by the PICAM sensor.

If MPO is not in the dayside mid-latitudes, PICAM, thanks to its wide FOV, can help in the detection of CME effects by detecting the SW circulation inside the magnetosphere.

If MPO is in the night side, ELENA could infer a signature of strong SW flux blowing around the planet by remote sensing the charge-exchange ENA generated close to the limb (Mura et al., 2005). The signature of substorm generation caused by CME arrival can be proved by the detection of field-aligned fluxes (of SW originating particles as well as of planetary originating particles) (Slavin et al., 1997) by PICAM and MIPA. Simultaneously, STROFIO could detect the effects on the night side exosphere of the increased magnetospheric activities. In fact, we can expect that the enhanced exospheric density in the dayside will produce some intensification also in the night side due to the migration of particles (Killen et al., 2007). ELENA will detect the SHEA generated by the impact of loss-cone particles on the surface monitored by MIPA.

Thanks to the presence of particle and field packages on board both MPO and MMO satellites, the SW and IMF monitoring compared to particles and magnetic field signal observed from inside the magnetosphere will be very useful for the comprehension of the planetary response to SW variations. Such a two vantage points configuration will frequently occur during the mission. For instance, the two MMO–MPO vantage points simultaneous observations will allow to detect the spatial and temporal evolution of SW disturbances, when propagating inside the Hermean magnetosphere; on the other hand, even the surface emission under different SW conditions and the related exospheric characteristics will be monitored by the two satellites, rising evidence of possible dynamical processes occurring within the neutral gas surrounding the planet. These are just examples of the many joint tasks which will be performed by the plasma packages onboard the two satellites in the frame of magnetosphere–exosphere–surface coupling processes (an extended picture of possible joint measurements of the BepiColombo mission is given in Milillo et al., 2009).

Comparison of the charge-exchange ENA measurements recorded by MPO/SERENA–ELENA and by MMO/MPPE–ENA in the Mercury environment with those achieved by ENA imagers already flying around Earth (IMAGE), Mars (Mars Express), Venus (Venus Express), and Saturn (Cassini) will allow comparative investigations of evolution and dynamics of planetary magnetospheres.

As already stated in Section 1.2.4, the yield of the heavy-ion sputtering is higher with respect to the proton sputtering; nevertheless, due to the low heavy-ion flux inside the SW, the neutral/ion release in this case is probably lower (Delcourt et al., 2003; Delcourt and Seki, 2006) than the release due to the sputtering of the major SW components (protons and alpha particles). However, at the night side where the effectiveness of other release processes is very low, and heavy ionized particles of planetary origins are expected to impact onto the surface, the sputtered products could be possibly detectable. Delcourt et al. (2003) estimated the sputtered Na signal up to $10^4\,cm^{-2}\,s^{-1}$. The neutral signal during intense precipitation events could be identified by ELENA.

2. SERENA instrument package

The energy spectrum of neutral particles ranges from fractions of eV up to several keV. Such a large energy interval cannot be covered by a single detector (Wurz, 2000). The SERENA instrument is, therefore, based on a modular approach comprising four sensors:

- the STROFIO sensor measures the neutral particle composition at the lowest energy range (~0 to a few eV), and the particle density in the exosphere;
- the ELENA sensor covers the $<20\,eV$–$5\,keV$ energy spectrum.

The STROFIO sensor measures the neutral particles with low energies (exospheric particles) and has no imaging capability, i.e. no angular resolution. The analysis of the exospheric released gases allows indirect reconstruction of

Table 1
SERENA units major characteristics.

	STROFIO	ELENA	PICAM	MIPA
Energy range	<1 eV	<0.02–5 keV	0.001–3 keV	0.01–15 keV
Resolution	–	$\Delta v/v$: $\approx 10\%$	$\Delta E/E$: 10%	$\Delta E/E$: 7%
FOV, deg.	20×20	4.5×76	3D: hemisphere	2D: 9×180
Resolution, deg	–	4.5×2.4	22.5×22.5	4.5×22.5
Mass resolution	$M/\Delta M > 60$	H and heavy species	$M/\Delta M > 60$	$M/\Delta M \sim 5$
Geom. factor (total)	0.14 (counts/s)/(particles/cm^3)	$\sim 6 \times 10^{-4}$ (cm^2 sr)	$\sim 3.4 \times 10^{-3}$ (cm^2 sr)	$\sim 1.8 \times 10^{-3}$ cm^2 sr eV/eV
Efficiency		Ener. dep.:$\sim 5 \times 10^{-3}$–0.5	Energy dep.	1–10% (adjustable)

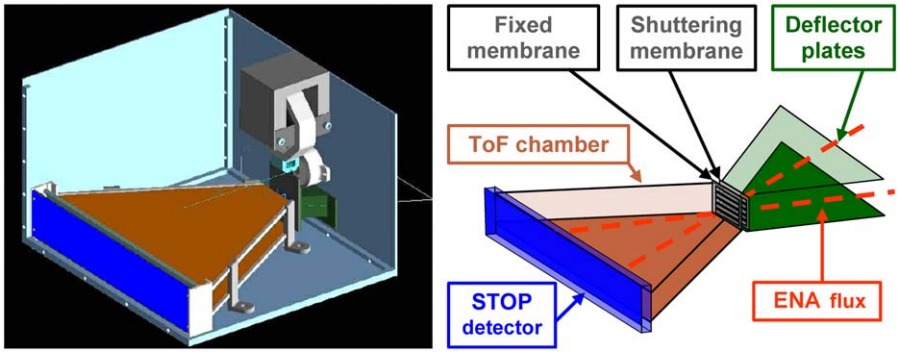

Fig. 5. ELENA concept.

the surface composition, by processing successive measurements over several orbits.

The ELENA sensor has a high angular resolution and a nadir-pointing 1-D field-of-view (perpendicular to the S/C orbital plane). This configuration allows a subsequent collection of the ELENA observations along each single orbit for reconstructing the global image of the particle populations surrounding Mercury and its interaction with the surface.

The energy gap below 20 eV and above few eV is not covered for technological reasons, nevertheless no process that produces particles only within this energy range is foreseen, so that the related fluxes may be reconstructed by interpolating procedures.

The two ion spectrometers are complementary. The geometrical factor of MIPA is optimized for monitoring very high fluxes (up to 10^9 part/(cm^2 s sr)) of the precipitating SW and magnetospheric ions that may eventually induce the ion-sputtering process. PICAM with its higher mass resolution is optimized for measuring lower fluxes of exo-ionosphere, whereas MIPA, which is full-time devoted to the detection of SW precipitation, has wider energy range. Both sensors have good time resolutions and they will respond efficiently to abrupt and fast changes of the precipitating ion fluxes. In Table 1, the basic characteristics of the four units are listed.

2.1. ELENA

ELENA (see Fig. 5) is a time-of-flight (TOF) sensor, based on the state-of-the-art of ultrasonic oscillating choppers (operated at frequencies above 20 kHz and up to 100 kHz), mechanical gratings and micro-channel plate (MCP) detectors. The new development in this field allows unprecedented performance in timing discrimination against noise of low-flux neutral particles. The purpose of the chopping is to digitize space and time when tagging the incoming particles without introducing 'disturbing' detector elements, which may affect the trajectory and energy of the particles. This is particularly important in this case, where neutrals with energies of a few tens of eVs must be detected.

The sensor concept is based on a mechanical nano-shuttering system, which allows the incoming neutral particles impinging on the detector entrance (with an instantaneous FOV of $4.5^\circ \times 76^\circ$) with a definite timing. The nano-shuttering element consists of two self-standing silicon nitride (Si_3N_4) membranes, patterned with arrays of long and narrow openings, of the order of 100 nm, one facing the other. These nano-slits are fabricated by electron beam lithography (EBL) and other techniques typically used for microelectronics. A piezoelectric ultrasonic actuator will be used for oscillating the shutter, with frequency ranging up to 100 kHz. Particles passing through the openings (occurring when the slits of two oscillating membranes are aligned, thus identifying the START time) are then flown in a TOF chamber, and are finally detected by a 1-D array (based on MCP and discrete anode sets), allowing to reconstruct both the velocity and the direction of the incoming particles. The width of each cut opening provides the latitudinal 4.5° FOV, whereas the 76° azimuthal FOV of the pinhole camera can be resolved into a series of 32 $4.5^\circ \times 2.4^\circ$-wide bins by means of discrete

anode sets in the MCP back. In general, the mass of neutrals is not identified, but it is possible to use information about the pulse-height on the MCP to discriminate a few mass channels, when it works in a proportional regime.

The total moving assembly (basically consisting of one of the two membranes and the related frame) has a mass of a few grams. The composite radiation made by neutrals, ions and light fluxes impinges onto the ELENA sensor entrance through an equivalent aperture of about 1 cm^2. The first IR stopping grid reflects unwished infrared (IR) radiation for minimizing the instrument heat loading. The metallic meshes of the grid are about $1 \times 4\,\mu m^2$, and they have transparency for the neutral particles of the order of 50%. Concerning sunlight, the adopted 2-μm-thick membranes with Si_3N_4 layers are almost completely opaque, so that generally, transparency is well below 10^{-28}. As far as the grid structure transmission is concerned, a specific simulation was used to evaluate the leakage, and it was found that each cut drops the entrance intensity of a factor less than 10^{-8}. In addiction, ion-deflecting plates are foreseen, located inside the TOF chamber. To observe the limb during apoherm passages, the linear array of ELENA angular pixels is shifted 8° in the perpendicular to the S/C orbital plane towards anti-radiator direction. Table 2 reviews the major ELENA characteristics. More details about ELENA are given by Orsini et al. (2008).

Table 2
ELENA major characteristics.

Energy range	<0.02–5 keV (mass dependent)
Velocity resolution $\Delta v/v$	Down to 10%
Viewing angle	$4.5° \times 76°$
Nominal angular resolution	$4.5° \times 4.5°$ (actual pixel)
	$4.5° \times 2.4°$ (nominal pixel)
Mass resolution, $M/\Delta M$	H and heavy species
Minimum integration time	40 s
Geometrical factor G	$\sim 2 \times 10^{-5}$ cm^2 sr
Integral geometric factor	$\sim 6 \times 10^{-4}$ cm^2 sr

2.1.1. ELENA signal simulation

The energetic neutral particles that are likely to be detected by ELENA come primarily from ion-sputtering process, and secondarily from charge exchange (Mura et al., 2005). To estimate the neutral flux measured by the instrument, we assume that, during an intense SW activity, a total of 5×10^{26} protons per second impact onto the surface (Leblanc et al., 2003, and references therein). These protons impact on roughly 50% of the dayside surface and they cause the sputtering of various surface components, with a yield (Y) that is, on average, about 0.05 neutral particles for each incoming proton (Lammer et al., 2003), even if it depends on the surface neutral species considered. Because of the low abundance of heavy ions in the solar wind their contribution to the sputtered flux is negligible in normal conditions and only alpha particles contribute to the sputtered signal (about 30% to the total sputter yield; Wurz et al., 2007). During CME events the alpha and heavy particle abundances in the solar wind can increase (Wurz et al., 2003), thus, in this case, they can contribute to the process in a similar amount of protons (Johnson and Baragiola, 1991; Kallio et al., 2008).

In summary, a maximum ENA flux F of the order of 10^8 cm^{-2} s^{-1} sr^{-1} may be assumed at MPO periherm. The atomic composition of the neutral flux roughly corresponds to that at the surface. The fraction of back-scattered particles is between 0.1% and 1% of the impinging beam. Most of them are neutralized, since the charge-exchange mean free path inside the sample (of the order of 1 nm) is small compared to the mean depth of the back-scattering site (of the order of 1 m). The estimated neutral back-scattered total flux at MPO orbit, considering a yield of 1%, is about 10^7 (cm^2 s sr)$^{-1}$.

In the Hermean environment the charge-exchange neutrals have energies of the order of 1 keV, and they are expected to be primarily H-ENAs. The maximum estimated H-ENA flux is about 10^6–10^7 cm^{-2} s^{-1} sr^{-1} (Mura et al., 2005).

Fig. 6 shows an estimation of the count rates related to neutral fluxes that can be measured by ELENA during an

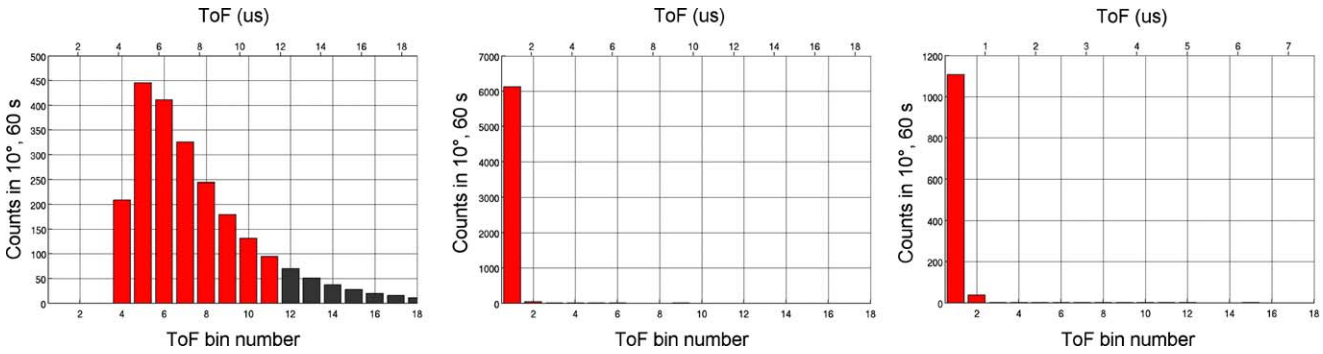

Fig. 6. Left panel: analytical prediction of the sputtered signal (red columns) measurable by ELENA and particles arriving after the new opening (gray columns). Gray channels are "virtual", since their counts are actually collected in channels 1–5. Middle panel: signal prediction for back-scattered particles. Right panel: signal prediction for charge-exchange particles.

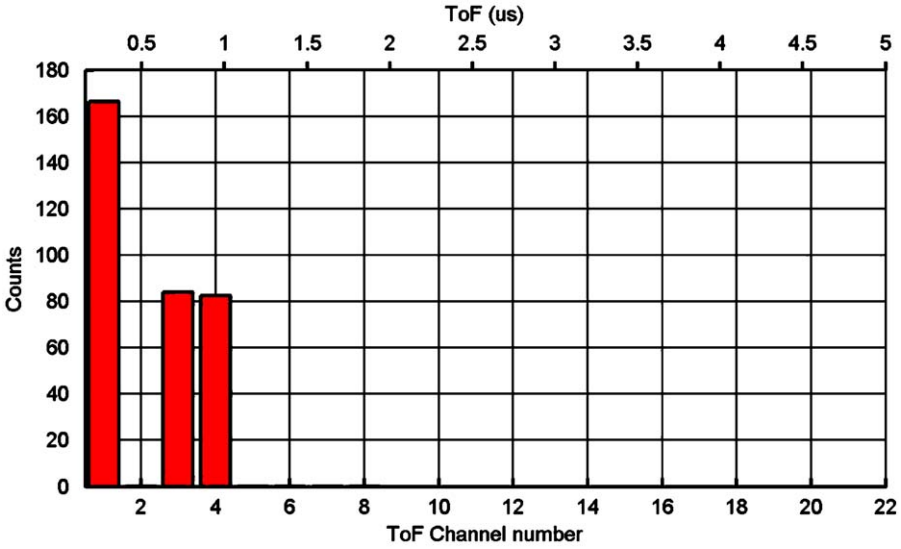

Fig. 7. ELENA mass resolution capability based on ToF analysis. Simulation of two laboratory H- and O-ENA fluxes with similar energy distributions (~1 keV). The shutter frequency has been set to 100 kHz. The peak in the first channel is H, whereas the peak in channels 3–4 is due to O (from Mura et al., 2007b).

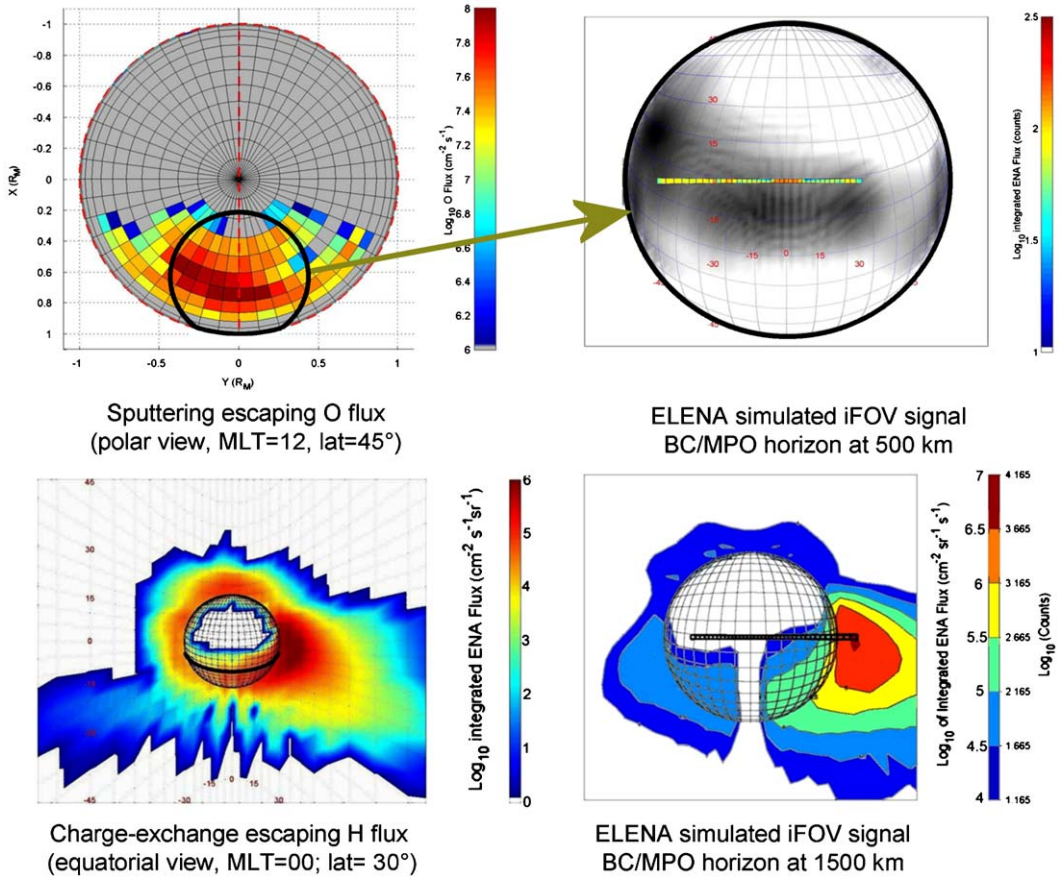

Fig. 8. ELENA signal simulation: ion-sputtering (top panels) and charge-exchange (bottom panels. Left column: theoretical predictions; right column: ELENA signal simulations.

intense ion-sputtering and back-scattering event left and middle panels, respectively. Fig. 6 right panel shows the charge-exchange estimated signal as can be seen by ELENA. We have estimated the count rates in 11 useful TOF channels with a Monte Carlo model, simulating a sputtering distribution of a number of particles equal to T_{int}, G, F, n, where T_{int} is the time window, G is the geometrical factor, F is the flux at instrument entrance and

n is the number of angular sectors. We can see that the simultaneous observations of ion sputtering and back-scattering may be easily discriminated, given the ELENA TOF resolution. The charge-exchange signal has different origin and direction; hence, it is always discriminated with respect to the signal due to back-scattering.

The ELENA TOF capability implies a limited possibility to discriminate light with respect to heavy species. In Fig. 7 we show a demonstrative simulation of such a kind of analysis, which indicates that H- and O-ENA fluxes with similar energy distributions (~1 keV) are discriminated through TOF analysis (see figure caption for details). The expected signal at Mercury is composed by SHEA (mainly heavy atoms at lower energies) and H-ENAs; these two populations are even more separated in TOF spectra, and hence are easily discriminated as well. Furthermore, the expected look directions of H-ENAs and sputtered particles are different.

Since the real conditions at Mercury are not known, ELENA will maintain the possibility to have a spatial resolution of $2^\circ \times 2^\circ$, allowing an imaging of the surface with resolution between 15 and 70 km (for peri and apoherm, respectively). In Fig. 8 (top left panel), we show a simulation of the energy-integrated (between 20 and 1000 eV) sputtered O from vantage point close to the periherm on the day side. The instantaneous FOV of the linear array of the ELENA sensor is shown as a slice in the top right panel. The edge sectors of the array, which will observe the limb when the MPO spacecraft will approach the apoherm, will observe ENA from charge exchange of SW with exospheric gas, providing insight into the SW circulation inside the Hermean magnetosphere (Mura et al., 2005). In Fig. 8 (bottom left panel), the energy-integrated H-ENA signal from the night side apoherm is shown. The instantaneous FOV of the ELENA linear array is shown as a slice in the bottom right panel. In this way, ELENA will be able to monitor the surface emissivity induced by sputtering with great angular detail, so that the local characteristics of emission could be resolved, and the mutual effects induced by surface

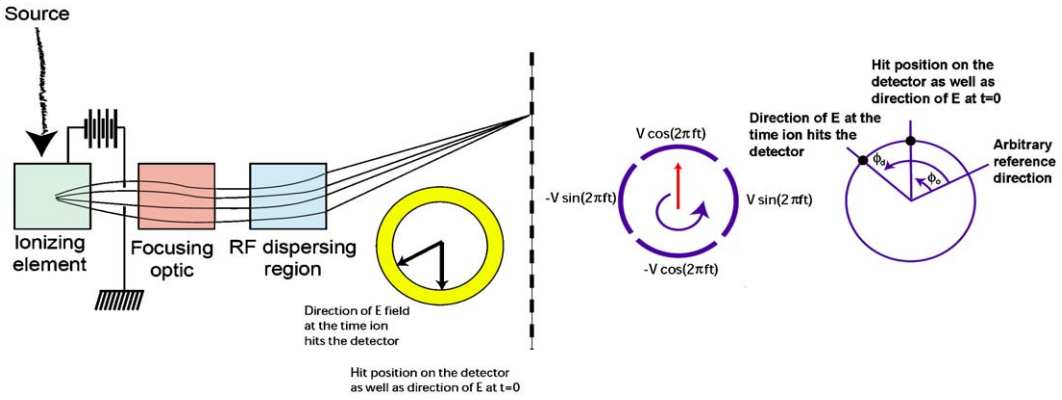

Fig. 9. Left: block diagram of sensor layout and example of trajectories. Right: STROFIO: functionality of the time rotating field.

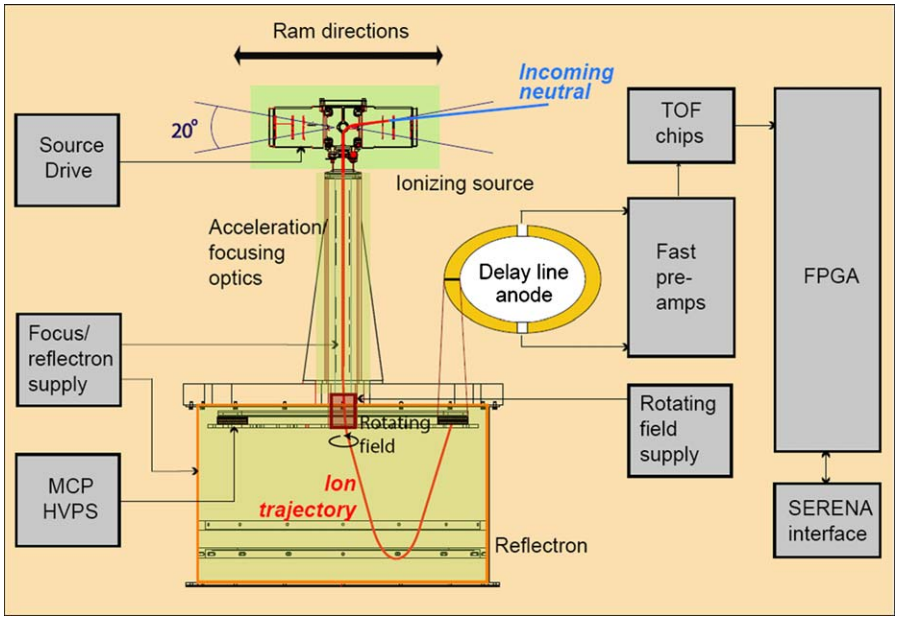

Fig. 10. STROFIO assembly block diagram.

sputtering capability (depending on local elemental composition) and ion precipitation intensity could be discriminated. Thanks to the MPO orbit, a full coverage of the surface under different ion precipitation conditions will be possible within the mission lifetime.

2.2. STROFIO

STROFIO is a mass spectrograph that determines particle mass per charge (m/q) by a TOF technique. The name comes from the Greek word *Strofi,* which means "to rotate": the phase of a rotating electric field "stamps" a start time on the particles' trajectory, and the detector records the stop time. STROFIO is characterized by a high sensitivity (0.14 counts/s when the density is 1 particle/cm^3).

Table 3
STROFIO major characteristics.

Energy range	<1 eV
Viewing angle (°)	20×20
Mass resolution, $M/\Delta M$	60
Mass range	1–64 Da (AMU)
Sensitivity	0.14 (counts/s)/(particles/cm^3)
Temporal resolution	10 s

The mass resolution ($m/\Delta m = 60$) is achieved by fast electronics and does not require tight mechanical tolerances. STROFIO is a novel type of mass spectrometer: the start time is imprinted on the trajectory of the particle by a radio frequency electric field, that bends the trajectory in a given plane, and the stop time is the time when the particle reaches the detector. Every particle is analyzed by the system, thus dramatically increasing the total sensitivity of the mass spectrometer. Moreover, its performances depend on fast electronics rather than on mechanical tolerances, making this type of sensors mechanical simple and easy to operate. The neutral gas enters into the ionization chamber through the entrance in the ram direction (see Figs. 9 and 10), after which it is ionized and accelerated into the mass analyzer. Here the ions experience the effects of an electric field, constant in magnitude, but with direction rotating uniformly in space, in a plane perpendicular to the initial ion velocity, at a frequency f. The trajectory of an ion can hit the detector only if the field points to the detector, while the ion traverses the dispersing region. At other times, the ion will simply miss the detector. The time difference between the instant when the particle arrives at the detector and the time when the field was pointing in the appropriate direction is equal to the travel time through the field free

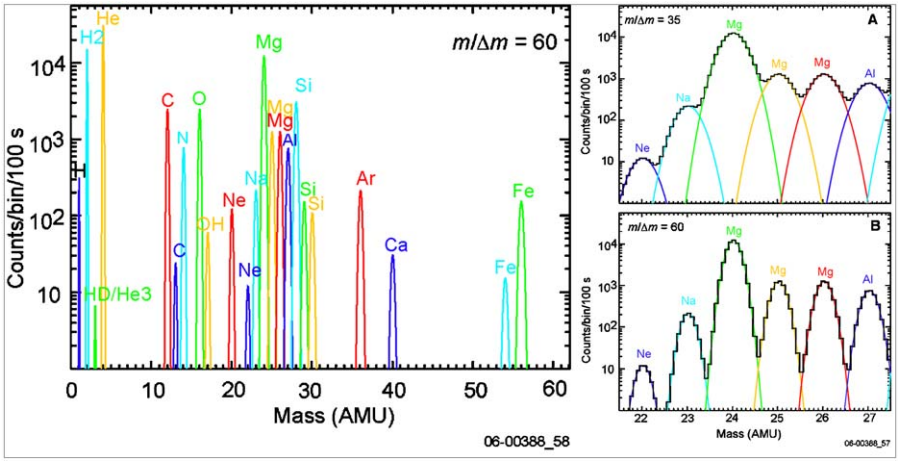

Fig. 11. Test of the STROFIO prototype. Mass composition is typical of rest gas in the vacuum chamber.

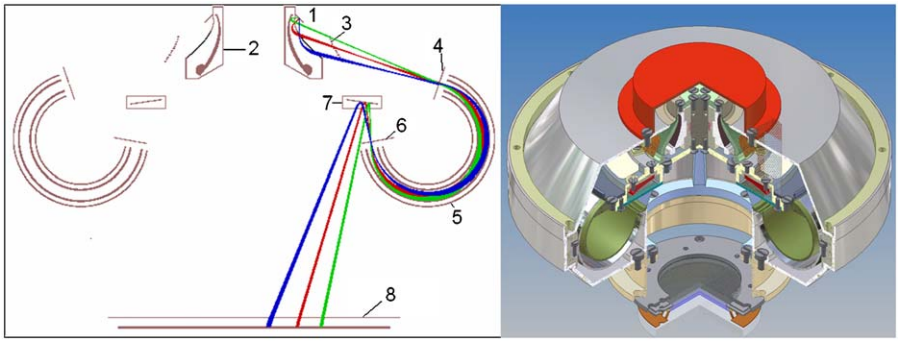

Fig. 12. Left: PICAM configuration with entrance window (1), primary mirror (2), gate (3), secondary slit (4), toroidal analyzer (5), exit slit (6), mirror (7), and MCP detector (8). Ion beams with entrance polar angles 0°, 45°, and 90° are shown in green, red, and blue, respectively. Right: Cross section of the PICAM sensor optics.

region. In Table 3 the major STROFIO characteristics are summarized.

2.2.1. STROFIO signal simulation

The particles released from the surface flow along ballistic orbits, and then, if their energy is lower than the escape one, they may fall down on the planet surface. STROFIO will 'capture' these particles along the satellite ram direction, thus allowing a precise estimate of the mass composition. Generally, most of the major species expected densities are sufficiently high to be detected by STROFIO (see Killen and Ip, 1999; Milillo et al., 2005).

Fig. 11 shows a result obtained during a test of the STROFIO prototype. The spectrum shows the mass composition of the residual gas in the chamber, thus giving confidence with the expected quality of mass discrimination capability, thanks to the STROFIO high sensitivity (see Table 3).

2.3. PICAM

PICAM operates as an all-sky camera for charged particles (Vaisberg et al., 2001) allowing the determination of the 3D velocity distribution and mass spectrum for ions over a full 2π FOV, from thermal up to ~3 keV energies and in a mass range extending up to ~132 AMU (Xenon). The instantaneous 2π FOV coupled with this mass range and a mass resolution better than ~50 is a unique capability, which provides to PICAM superior performances in the frame of the MPO mission. Fig. 12 shows a general layout of the sensor in order to obtain a 2π field of view. The ion optics is based on the principle of a modified pinhole camera. The sensor is symmetric along the Z-axis and its FOV is a hemisphere centered along this axis. Ions enter through an annular slit. After reflection on an ellipsoidal ion mirror the 90° polar angle distribution is folded into a 15° angular range. Here the ions pass a modulated wire gate that defines discrete packets of ions for analysis of the TOF until the particles impact on the MCP. The modulation can be either single shot or with a pseudo-random sequence which results in higher efficiency. After energy selection in a toroidal analyzer, particles enter the TOF and imaging section. A cross section of the ion optics is shown in Fig. 12, right panel. UV rejection will be obtained by a striated primary mirror covered by a non-reflecting layer of Cu_2S, which decreases the UV reflection by a factor of 1000. Multiple reflections within the instrument, the small entrance slit and the narrow exit slit (6) in front of the mass analyzer provide very strong protection. PICAM is a single unit consisting of the sensor and an attached electronics box, which interfaces to the external electronics. The outer part of the ion optics is designed for hot conditions. The lower part of the sensor containing the MCPs and the detector electronics is thermally decoupled. The specific PICAM electronics includes dedicated low- and high-voltage power supplies, detector, coordinate determination and gating electronics, and an FPGA-based controller. Table 4 summarizes the PICAM major characteristics.

Table 4
PICAM major characteristics.

Energy range	1 eV–3 keV
Energy resolution $\Delta E/E$	10%
Viewing angle	3-D, 2π
Angular resolution	~22.5°
Mass resolution, $M/\Delta M$	>60
Mass range	1…~132 AMU (Xe)
Time resolution	1–32 s
Geometrical factor $G = S\Omega$	3.4×10^{-3} cm^2 sr

2.3.1. PICAM signal simulation

Delcourt et al. (2003) showed that the ions trapped at low altitudes in the magnetic field of Mercury are drifting with velocities determined by the configuration of the magnetic and electric fields. The convection process results in localized ion populations, which may be accelerated to energies of several keV. By using this model for describing the production and transport of neutral and ionised Na atoms around Mercury, Leblanc et al. (2003) derived the

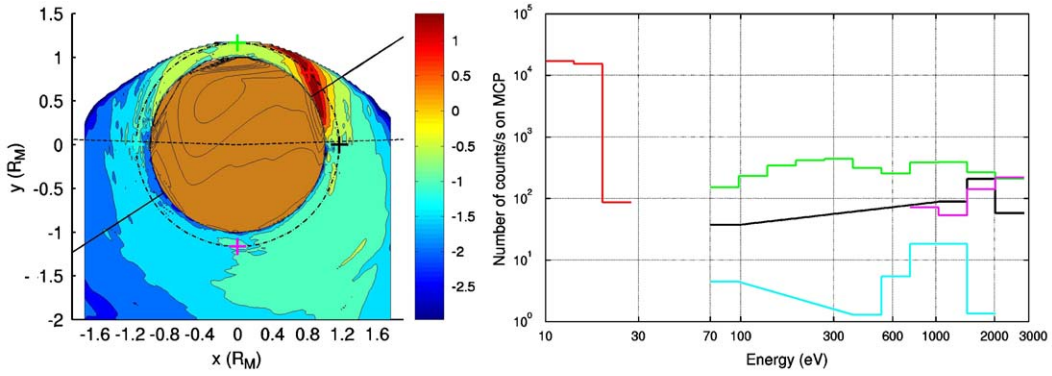

Fig. 13. Left: Na^+ density distribution in Log_{10} of Na^+/cm^3 calculated by Leblanc et al. (2003) at TAA = 150° and in the equatorial plane. This calculation is done for average and idealized solar wind conditions. The dashed circle indicated an altitude of 400 km and the five crosses the positions at which the calculation of the signal measured by PICAM have been done. Right: PICAM count rate in an omnidirectional mode. The different curves correspond to the different positions indicated by crosses in left panel (same colors).

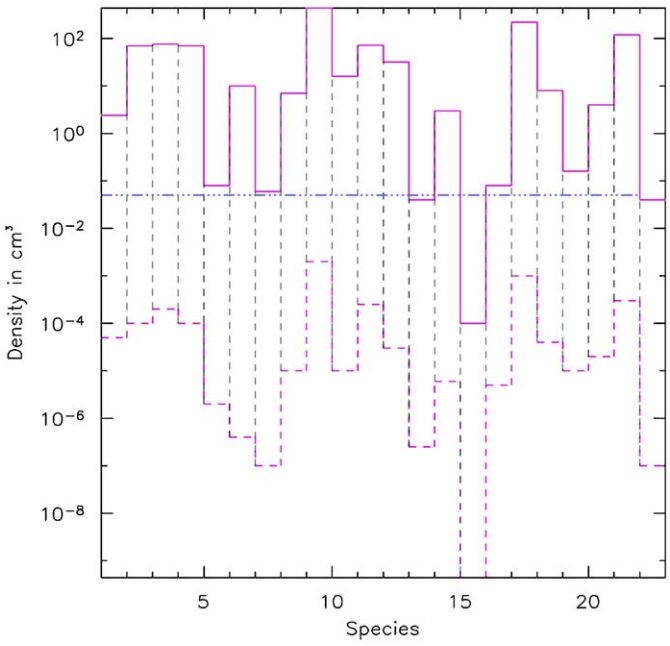

Fig. 14. Range of expected densities at 400 km in altitude for the main ions thought to be present in Mercury's ion exosphere. Also indicated is the threshold of detection for PICAM at the satellite velocity (dashed black line). We underlined the case of the Na^+, which has been discussed previously as a source of comparison to the other ions. The name of the ion is indicated. The solid line corresponds to the highest density expected and the dashed line for the lowest one (from Leblanc et al., 2004).

Na^+ distributions that can be expected at different positions around Mercury (Fig. 13, left) from which PICAM count rates can be calculated (Fig. 13, right). The simulations show that different energy distributions are expected along the MPO orbit. In particular, signal intensification occurs in the post dawn sector and the distribution exhibits rather low energies with respect to other locations (the exo-ionosphere in this case is constituted by newly born photoionized ions). It is to be noted here that Na^+ ions are expected to be a relatively minor fraction of the ion population and therefore the count rates for most of the other ion species will be significantly higher. The estimates of the ion density are highly variable depending on assumptions. In Fig. 14, the range of estimated densities at 400 km of altitude is shown for many species (Mg^+, O^+, C^+, N^+, Al^+, Si^+, S^+, Fe^+ and Ni^+) (Leblanc et al., 2004). The PICAM sensitivity is sufficient to perform significant measurements.

2.4. MIPA

MIPA is a simple ion mass analyzer optimized to provide monitoring of the precipitating ions using as little spacecraft resources as possible. The energy range and mass range of the analyzers are optimazed so that it is capable to measure all main groups of ions present in the magnetosphere. The ion flux arrival direction is analyzed by two opposite emispherical cuts, properly high voltage biased to resolve the elevation angle of the incoming

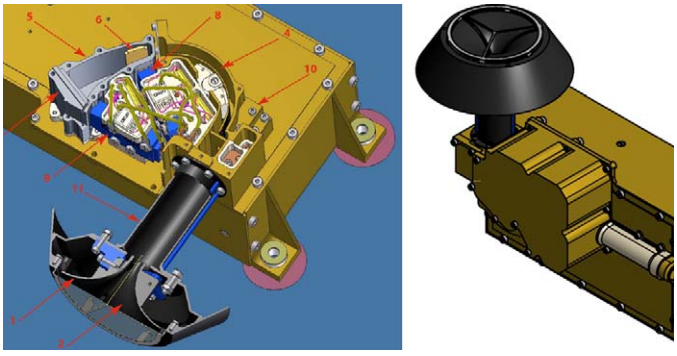

Fig. 15. Left panel: MIPA schematics with details numbered: deflector plates (1, 2, 3), electrostatic analyzer (4), TOF cell (5), START and STOP surfaces (6, 7), START and STOP CCEMs (8, 9), UV trap (10), thermal decoupling tube (11). Right panel: MIPA sensor view.

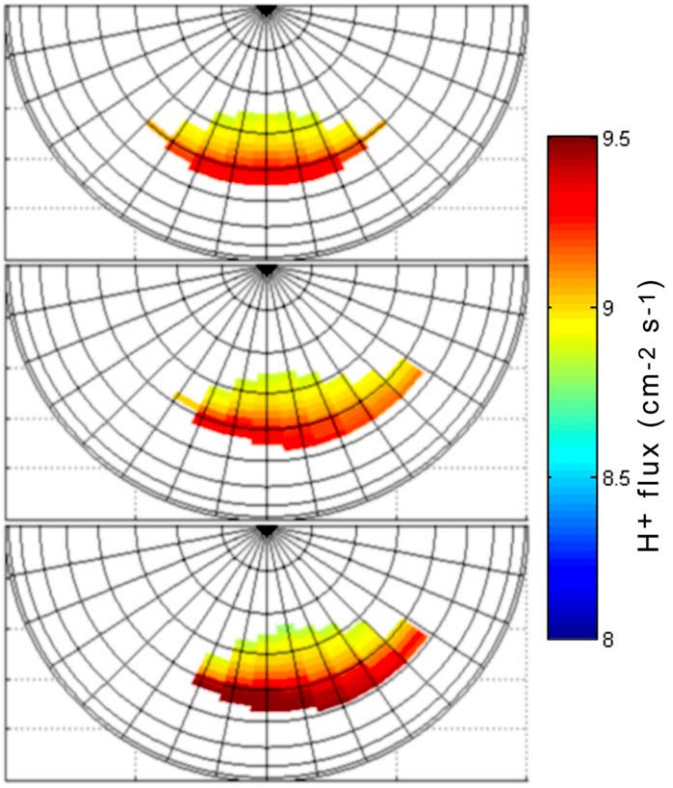

Fig. 16. Color-coded H^+ fluxes $[(cm^{-2}\,s\,sr\,keV)^{-1}]$ precipitating on the northern dayside surface of Mercury under different solar wind conditions. The three panels refer to: $P_{dyn} = 16$ nPa, $B_y = 0$ nT and $B_z = -10$ nT (top panel), $P_{dyn} = 16$ nPa, $B_y = -5$ nT and $B_z = -10$ nT (middle panel), $P_{dyn} = 60$ nPa, $B_y = -5$ nT and $B_z = -10$ nT (bottom panel) (Massetti et al., 2003).

particles. The azimuthal direction is achieved by mechanically sectoring the effective biasing section. The direction discriminating section is followed by a 128° double focusing cylinder electrostatic analyzer. The ions exiting the energy analyzer are post-accelerated up to 1 keV energy by a voltage applied to a ToF cell. Inside the cell, ions hit START and STOP surfaces producing secondary electrons

Table 5
MIPA major characteristics.

Energy range	15 eV–15 keV
Energy resolution $\Delta E/E$	7%
Viewing angle	$9^\circ \times 360^\circ$ 4 polar × 6 azimuth pixels
Angular resolution	$22.5^\circ \times 60^\circ$ (polar × azimuth
Mass range, amu	1–50
Mass resolution, $M/\Delta M$	~5
Time resolution, sec	8 s, 4 polar × 6 azimuth × 96 energy steps
Efficiency, ε	1–10%
Geometrical factor	10^{-5} cm^2 sr eV/eV per pixel, w/efficiency

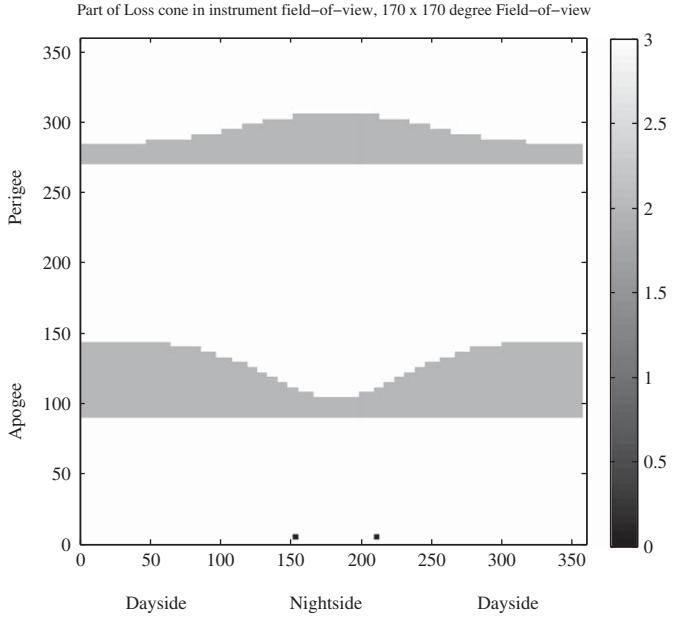

Fig. 17. Loss cone within the instrument field of view as a function of the spatial position given as true anomaly along the orbit (the y axis) and of the angle between the apocenter direction and the Mercury - Sun line. Light gray areas show that one of the angles either azimuth or elevation is outside the MIPA field of view. The white areas show the loss cone inside the MIPA field of view.

recorded by two ceramic channel electron multipliers giving respective timing. For energies above 4 keV, the post-acceleration is switched off. The timing of the event gives the ion velocity and, in combination with known energy, the mass. Fig. 15 shows the MIPA principle elements and the overall view. The geometrical factor of MIPA can be controlled by changing the post-acceleration voltage resulting in a change of the impact energy and thus secondary electron yield from the START and STOP surfaces, and reducing the size of the aperture slits. The maximum possible geometrical factor given by optimization of all parameters is too high for the Mercury conditions (see simulated fluxes in Fig. 16). The *G*-factor to be implemented in the sensor (base line) must be lowered with respect to the available one, in order to avoid countrates saturation. Table 5 lists the major MIPA characteristics.

2.4.1. MIPA signal simulation

With reference to the SW plasma entry into the Hermean magnetosphere, Massetti et al. (2003) noticed that most of the energy of the precipitating magnetosheath particles (and flux estimated around 10^8 cm^{-2} s^{-1} sr^{-1}) are deposited in a region that is narrow in latitude, but conversely extended in longitude. A typical open field area of Mercury's cusps during moderate south-ward pointing IMF, under the assumption of a typical SW pressure of 16 nPa at 0.39 AU ranges between about 45° and 65° in latitude, and about −40° and 40° in longitude (Fig. 16). Different IMF orientations, SW conditions and electric field action cause the open area to shift in latitude and longitude, and to vary its extension (Sarantos et al., 2001; Kallio and Janhunen, 2004; Mura et al., 2005). This intense flux of SW protons toward the planet will be monitored by MIPA. The magnetic field configuration near Mercury is poorly known and the planetary dipole field is highly deformed because of the SW interaction. Hence, the evaluation of the footprint of precipitating particles towards the surface is difficult, especially in the presence of large pressure variation and related modifications of the Mercury's MHD cavity. Because of the low-altitude orbit, MPO is the only platform useful for measuring and characterizing the amount of SW particles (Killen et al., 2004b; Massetti et al., 2003) as well as the heavier ions of planetary origin (Delcourt et al., 2003) that actually enter in the loss cone and, eventually, hit the planetary surface. In summary, MIPA will measure the flux of loss-cone-precipitating particles at Mercury (Fig. 17), which through ion sputtering will be a source of neutral and ion emission. The identification of the composition and energy distribution of the planetary ion flux impacting the surface can be achieved by the joint analysis of MIPA and PICAM.

3. Conclusions

In order to successfully perform the observations, the SERENA units are based on novel concepts for particle instrumentation, potentially interesting for future planetary missions beyond BepiColombo. SERENA constitutes the only particle package on board the BepiColombo-MPO. Thanks to the measurements provided by SERENA, a comparison with similar measurements taken on board the JAXA MMO satellite will be allowed. MMO is a spinning polar-orbiting satellite with an orbit of 400 by 12,000 km; it will carry instrumentation essentially devoted to the study of the Hermean Magnetosphere. The SERENA measurements will also complement other payload elements on board MPO devoted to environmental studies, like MAG (magnetic field), SIXS (solar radiation and energetic particles), and PHEBUS (UV exospheric emission).

Acknowledgements

The authors thank the two referees for corroborating this paper with very useful comments and suggestions. SERENA is primarily supported by the Italian Space Agency, Contract no. I/090/06/0, with contributions of other international partners for the provision of STROFIO, PICAM, and MIPA.

Appendix A. SERENA team members

- Executive

  S. Orsini[2] (Principal Investigator), S. Livi[3] (Co-PI, STROFIO), K. Torkar[4] (Co-PI, PICAM), S. Barabash[5] (Co-PI, MIPA), A. Milillo[2] (PI Deputy, Science Coordinator), P. Wurz[6] (Leading Co-I, Science Coordinator), A.M. Di Lellis[7] (Project Manager), E. Kallio[8] (Leading Co-I, Data distribution).
- Other Co-I's and Team Members

  G. Ho (Leading Co-I)[9], J. Kasper[10] (Leading Co-I), S. McKenna (Leading Co-I)[11], O. Vaisberg (Leading Co-I)[12], F. Allegrini[3], H. Andersson[5], C. Aoustin[13], K. Asamura[14], L. Avanov[12], V. Babkin[12], J. Balaz[11], M. Balikhin[15], S. Balint[16], W. Baumjohann[4], W. Benz[6], J.J. Berthelier[17], H. Biernat[4], P.C. Brandt[9], R. Bruno[2], J. Burch[3], M.T. Capria[18], M.G. Castellano[19], R. Cerulli-Irelli[2], M.R. Collier[20], G. Cremonese[21], D. Crider[22], C. C. Curtis[23], R. D'Amicis[2], I.A. Daglis[24], I. Dandouras[13], E. De Angelis[2], A. De Los Santos[3], D. Delcourt[17], M. Delva[4], M. Desai[4], S. Di Cosimo[24], L. Duvet[25], P. C. Escoubet[25], M. Fama[26], A. Fedorov[13], L. Ferrari[27], M. Fraenz[28], G. Fremuth[4], M. Genzer[8], A. Gnoli[27], R. Goldstein[3], M. Grande[29], V. Grishin[12], R. Gurnee[9], D.K. Haggerty[9], K. Heerlein[28], I. Hernyes[16], M. Holmström[5], K.C. Hsieh[23], W.H. Ip[30], A. Lacques[9], H. Jeszensky[4], R. Johnson[26], K. Kecskemety[16], R. Killen[31], G. Koynash[12], N. Krupp[28], K. Kudela[32], S. Lajos[16], H. Lammer[4], G. Latini[27], Francois Leblanc[17], Frederic Leblanc[33], A. Leibov[12], R. Leoni[19], H. Lichtenegger[4], C. Lipusz[16], A. Loose[28], P. Louarn[13], R. Lundin[5], A. Mälkki[8], V. Mangano[2], S. Massetti[2], F. Mattioli[19], D. McCann[5], D.J. McComas[3], D.G. Mitchell[9], T.E. Moore[20], A. Morbidini[2], A. Mura[2], H. Nilsson[5], M. Oja[5], R. Orfei[2], I. Panagopoulos[24], D. Piazza[6], F. Pitout[34], C. Pollock[3], S. E. Pope[3], G. Prattes[4], H. Rème[10], P. Riihelä[8], R. Rispoli[2], E.C. Roelof[3], J. Rynö[8], M. Sarantos[31], J. A. Sauvaud[13], J. Scheer[6], W. Schmidt[8], K. Seki[35], S. Selci[27], A. Skalski[12], J.A. Slavin[20], J. Svensson[5], S. Szalai[16], K. Szego[16], D. Toublanc[10], P. Travnicek[36], N. Vertolli[2], P. Wahlström[6], S. Wang[14], M. Wedlund[37], M. Wieser[5], J. Woch[28], S. Zampieri[2].

[2]INAF/IFSI, Roma, Italy.
[3]SwRI, San Antonio, TX USA.
[4]IWF, Graz, Austria.
[5]IRF, Kiruna, Sweden.
[6]University of Bern, Bern, Switzerland.
[7]AMDL s.r.l., Roma, Italy.
[8]FMI, Helsinki, Finland.
[9]JHU/APL, Laurel, MD USA.
[10]SAO, Cambridge, MA USA.
[11]National University of Ireland, Maynooth, Ireland.
[12]IKI, Moscow, Russia.
[13]CESR, Toulouse, France.
[14]ISAS, Kanagawa, Japan.
[15]Sheffield University, UK.
[16]KFKI, Budapest, Hungary.
[17]CETP, Saint Maur d.Fossës, France.
[18]INAF-IASF, Roma–Italy.
[19]CNR–IFN, Roma, Italy.
[20]NASA/GSFC, Greenbelt, MD USA.
[21]INAF-OAP, Padova, Italy.
[22]CUA, Washington, DC USA.
[23]University of Arizona, Tucson, AZ USA.
[24]NOA, P. Penteli, Greece.
[25]ESA/ESTEC, Noordwijk, The Netherlands.
[26]University of Virginia, Charlottesville, VA USA.
[27]CNR–ISM, Roma, Italy.
[28]MPS–MPI, Lindau, Germany.
[29]RAL, Oxfordshire, England.
[30]NCU, Taoyuan, Taiwan.
[31]University of Maryland, College Park, MD USA.
[32]IEP-SAS, Košice, Slovakia.
[33]IPSL, Verrieres-Le-Buisson, France.
[34]LPG, Saint-Martin d'Heres, France.
[35]STELAB –Nagoya University, Toyokawa, Japan.
[36]UFA-CAS, Prague, Czech Republic.
[37]Service d'Aeronomie, Paris, France.

References

Chassefiere, E., et al., 2009. PHEBUS: A double ultraviolet spectrometer to observe Mercury's exosphere. Planet. Space Sci. 56, 201–223.
Delcourt, D.C., Seki, K., 2006. On the dynamics of charged particles in the magnetosphere of Mercury. Adv. Geoscience 3, 17.
Delcourt, D.C., Grimald, S., Leblanc, F., Berthelier, J.-J., Millilo, A., Mura, A., Orsini, S., 2003. Ann. Geophys. 21, 1723.
Fjelbo, G., Kliore, A., Sweetnam, D., Esposito, P., Seidel, B., Howard, T., 1976. The occultation of mariner 10 by Mercury. Icarus 29, 407–415.
Ip, W-H., 1997. Time-variable phenomena in the magnetosphere and exosphere of Mercury. Adv. Space Res. 19, 1615.
Johnson, R.E., Baragiola, R., 1991. Geophys. Res. Lett. 18 (11), 2169.
Kabin, K., Gombosi, T., DeZeeuw, D., Powell, K., 2000. Interaction of mercury with the solar wind. Icarus 143, 397–406.
Kallio, E., Janhunen, P., 2003. Solar wind and magnetospheric ion impact on Mercury's surface. Geophys. Res. Lett. 30 (17), 1877.
Kallio, E., Janhunen, P., 2004. The response of the Hermean magnetosphere to the interplanetary magnetic field. Adv. Space Res. 33 (12), 2176–2181.
Kallio, E., Wurz, P., Killen, R., McKenna-Lawlor, S., Milillo, A., Mura, A., Massetti, S., Orsini, S., Lammer, H., Janhunen, P., Ip, W.-H., 2008. On the impact of multiply charged heavy solar wind ions ion the surface of Mercury, the Moon and Ceres. Planet. Space Sci. 56, 1506–1516.
Killen, R.M., Ip, W.-H., 1999. The surface-bounded atmosphere of Mercury and the Moon. Rev. Geophys. 37, 361.
Killen, R.M., Sarantos, M., Potter, A.E., Reiff, P., 2004a. Source rates and ion recycling rates for Na and K in Mercury's atmosphere. Icarus 171, 1–19.
Killen, R.M., Sarantos, M., Reiff, P., 2004b. Space weather at Mercury. Adv. Space Res. 33 (11), 1899.
Killen, R.M., Bida, T.A., Morgan, T.H., 2005. The calcium exosphere of Mercury. Icarus 173, 300.

Killen, R.M., Potter, A.E., Mura, A., Lammer, H., Cremonese, G., Wurz, P., Orsini, S., Milillo, A., Sprague, A.L., Khodachenko, M.L., Lichtenegger, H.I.M., 2007. Processes that promote and deplete the exosphere of Mercury. Space Sci. Rev. 9.

Lammer, H., Wurz, P., Patel, M.R., Killen, R., Kolb, C., Massetti, S., Orsini, S., Milillo, A., 2003. Icarus 166/2, 238.

Leblanc, F., Delcourt, D., Johnson, R.E., Liu, M., 2003. Mercury's sodium exosphere: magnetospheric ion recycling. J. Geophys. Res. 12, 5136.

Leblanc F., Lammer H., Torkar K., Berthelier, J.J., Vaisberg O., Woch, J., 2004. Notes du Pôle de Planëtologie de l'IPSL, No. 5.

Massetti, S., Orsini, S., Milillo, A., Mura, A., De Angelis, E., Lammer, H., Wurz, P., 2003. Mapping of the cusp plasma precipitation on the surface of Mercury. Icarus 166/2, 229.

Massetti, S., Orsini, S., Milillo, A., Mura, A., 2007. Modelling Mercury's magnetosphere and plasma entry through the dayside magnetopause. Planet. Space Sci. 55, 1557–1568.

Milillo, A., Orsini, S., Wurz, P., Delcourt, D., Kallio, E., Killen, R.M., Lammer, H., Massetti, S., Mura, A., Barabash, S., Cremonese, G., Daglis, I.A., De Angelis, E., Di Lellis, A.M., Livi, S., Mangano, V., Torkar, K., 2005. Surface–exosphere–magnetosphere system of Mercury. Space Sci. Rev. 117/3, 397–444.

Milillo, A., Fujimoto, M., Kallio, E., Kameda, S., Leblanc, F., Narita, Y., Cremonese, G., Laakso, H., Laurenza, M., Massetti, S., McKenna-Lawlor, S., Mura, A., Nakamura, R., Omura, Y., Rothery, D.A., Seki, K., Storini, M., Wurz, P., Baumjohann, W., Bunce, E., Kasaba, Y., Helbert, J., Sprague, A., Hermean Environment WG, 2009. The BepiColombo mission: an outstanding tool for investigating the Hermean environment Planet. Space Sci. 56, 40–60.

Mura, A., Orsini, S., Milillo, A., Delcourt, D., Massetti, S., De Angelis, E., 2005. Dayside H+ circulation at Mercury and neutral particle emission. Icarus 175, 305.

Mura, A., Milillo, A., Orsini, S., Massetti, S., 2007a. Numerical and analytical model of Mercury's exosphere: dependence on surface and external conditions. Planet. Space Sci. 55, 1569–1583.

Mura, A., Orsini, S., Milillo, A., Di Lellis, A.M., De Angelis, E., Massetti, S., 2007b. Numerical Simulation of ELENA performances; INAF/IFSI-2007-17 (Oct.).

Mura, A., Wurz, P., Lichtenegger, H.I.M., Schleicher, H., Lammer, H., Orsini, S., Milillo, A., Delcourt, D., Milillo, A., Orsini, S., Massetti, S., Khodachenko, M.L., 2008. The sodium exosphere of Mercury: comparison between observations during Mercury's transit and model results. Icarus, in press.

Orsini, S., Blomberg, L.G., Delcourt, D., Grard, R., Massetti, S., Seki, K., Slavin, J., 2007. Magnetosphere–exosphere–surface coupling at Mercury. Space Sci. Rev.

Orsini, S., Di Lellis, A. M., Milillo, A., De Angelis, E., Mura, A., Selci, S., Leoni, R., Mattioli, F., Orfei, R., Massetti, S., Dandouras, I., 2008. Low energy high angular resolution neutral atom detection by means of micro-shuttering techniques: the BepiColombo SERENA/ELENA sensor. In: Proceeding of the International Conference on Future Perspectives of Space Plasma and Particle Instrumentation and International Collaborations, Rikkyo Univ., Tokyo, Japan.

Potter, A.E., Killen, R.M., Sarantos, M., 2006. Spatial distribution of sodium on Mercury. Icarus 181 (1), 2006.

Sarantos, M., Reiff, P.H., Hill, T.W., Killen, R.M., Urquhart, A.L., 2001. A Bx-interconnected magnetosphere model for Mercury. Planet. Space Sci. 49, 1629.

Sarantos, M., Killen, R.M., Kim, D., 2007. Predicting the long-term solar wind ion-sputtering source at Mercury. Planet. Space Sci. 55, 1584–1595.

Sarantos, M., Killen, R.M., Sharma, A.S., Slavin, J.A., 2008. Correlation between Lunar Prospector measurements and the Lunar exosphere during passage through the Earth's magnetosphere. Geophys. Res. Lett. 35, L04105.

Schleicher, H., Wiedemann, G., Wöhl, H., Berkefeld, T., Soltau, D., 2004. Detection of neutral sodium above Mercury during the transit on 2003 May 7. Acta Astronaut. 425, 1119–1124, doi:10.1051/0004-6361:20040477.

Slavin, J.A., Owen, J.C.J., Connerney, J.E.P., Christon, S.P., 1997. Mariner 10 observations of field-aligned currents at Mercury. Planet. Space Sci. 45 (1), 133–141.

Vaisberg, O., Goldstein, B., Chornay, D., Keller, J., Avanov, L., Smirnov, V., Brinza, D., Croley, D., Sittler, E., Moore, T., Rozmarynowski, P., Fuselier, S., Ghielmetti, A., 2001. Ultra fast plasma analyser—an allsky camera for charged particles. ESA SP 493, 451–454.

Wurz, P., 2000. The Outer Heliosphere: Beyond the planets. In: Scherer, K., Fichtner, H., Marsch, E. (Eds.), Copernicus Gesellschaft e.V., Katlenburg-Lindau, Germany, p. 251.

Wurz, P., Lammer, H., 2003. Monte-Carlo simulation of Mercury's exosphere. Icarus 164 (1), 1.

Wurz, P., Wimmer-Schweingruber, R., Allegrini, F., Bochsler, P., Galvin, A., Ipavich, F.M., 2003. Solar Wind X. American Institute Physics, vol. 679, pp. 685–690.

Wurz, P., Rohner, U., Whitby, J.A., Kolb, C., Lammer, H., Dobnikar, P., Martÿn-Fernändez, J.A., 2007. Thelunarexosphere:thesputtering contribution. Icarus 191, 486–496.

Zurbuchen, T.H., Raines, J.M., Gloeckler, G., Krimigis, S.M., Slavin, J.A., Koehn, P., Killen, R.M., Sprague, A.L., McNutt Jr., R.L., Solomon, S.C., 2008. MESSENGER observations of the composition of Mercury's ionized exosphere and plasma environment. Science 321, 90.